

# INCONEL 718 SINGLE AND MULTIPASS MODELLING OF HOT FORGING

J. de Jaeger<sup>1,2,3</sup>, D. Solas<sup>2,4</sup>, T. Baudin<sup>2,4</sup>, O. Fandeur<sup>5</sup>, J-H. Schmitt<sup>1</sup> and C. Rey<sup>1</sup>

<sup>1</sup> MSSMAT, UMR 8579, Ecole Centrale Paris, 92290 Châtenay-Malabry, France

<sup>2</sup> Univ Paris Sud, ICMO, UMR 8182, F-91405 Orsay, France

<sup>3</sup> Forges de Bologne, 52310 Bologne, France

<sup>4</sup> CNRS, F-91405 Orsay, France

<sup>5</sup> CEA, DEN, DM2S, SEMT, LM2S, F-91191 Gif-sur-Yvette, France

Keywords: INCONEL 718, Forging, Dynamic Recrystallization, Crystalline Plasticity, Modelling

## Abstract

A better understanding of the competition between several mechanisms (dynamic recovery, dynamic recrystallization and plasticity hardening) is crucial for aircraft engine manufacturers. The aim of this paper is to improve the microstructure and therefore the mechanical properties of a nickel based superalloy used for rotating forged pieces. A nickel superalloy microstructure is the result of several successive hot forging processes: multipass processes, with intermediate dwell time and quenching. In this paper, an original three dimensional approach able to simulate these processes is proposed. The specific role of the different steps of the processes is analysed. In this approach, several forging thermo-mechanical parameters are taken into account: the working temperature, the strain rate, the final strain, the interpass time, etc. At high forging temperature, the studied INCONEL 718 presents an austenitic matrix  $\gamma$  (face centred cubic) assumed to be in a single phase.

This approach proposes a sequential coupling of two models, one devoted to deformation and the other to recrystallization. Such a coupling enables the estimation of the effect of deformation and of different recrystallization types on mechanical behaviour and on micro-structural evolution. The approach is performed at the grain scale and takes into account the whole thermo-mechanical cycle with a focus on the dynamic behaviour.

The first polycrystalline model is based on the plasticity mechanisms at the grains scale. The framework corresponds to finite transformations (large lattice rotations and small elastic strains). The model is implemented in ABAQUS and CAST3M finite element codes. The second model is based on the recrystallization theory and uses a 3D cellular automaton. It describes dynamic recrystallization phenomena such as nucleation-growth and static or post-dynamic recrystallization. Such recrystallization mechanisms were observed during interpass time or during the successive heatings depending on the thermo-mechanical paths used in multipass forging. Dislocation densities are the internal variables common to the two models. The simulations are performed on a 3D Representative Elementary Volume (aggregate) obtained from Electron Back Scattering mapping. Numerical results are compared to experimental microstructures.

## Introduction

INCONEL 718 is a nickel based superalloy hardened by nanometric precipitates such as  $\gamma''$  ( $\text{Ni}_3\text{Nb}$ ) and  $\gamma'$  ( $\text{Ni}_3(\text{Ti,Al})$ ). This alloy also contains a  $\delta$  ( $\text{Ni}_3\text{Nb}$ ) phase with an average size

which is hundred times larger than the  $\gamma''$  phase. This alloy is widely used for the aircraft engine applications.

The INCONEL 718 forging domain (Figure 1), is ranging between the melting point ( $T = 1150^\circ\text{C}$ ) determined by Lewandowski et al. [1] and the  $\gamma''$  phase solvus temperature ( $T = 940^\circ\text{C}$ ). Below the latter temperature, the nanometric precipitates harden the material, leading to excessive compression stresses during hot forging.

Within the optimal hot forging domain, the hardening phases are more or less dissolved according to their solvus temperatures (see Figure 1).

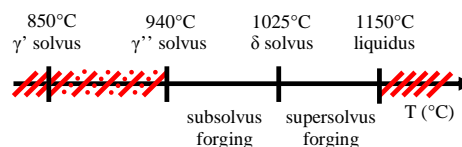


Figure 1: Forging domain of INCONEL 718

The forging domain is composed of two sub-domains located on each side of the  $\delta$  phase solvus temperature ( $T = 1025^\circ\text{C}$ ): the sub- $\delta$ -solvus domain below  $1025^\circ\text{C}$ , and the super- $\delta$ -solvus domain above  $1025^\circ\text{C}$ .

In the sub- $\delta$ -solvus domain the grain size is controlled by boundary pinning of precipitates. Forging in the sub- $\delta$ -solvus domain leads to a final fine grain size, while coarse grains are observed in the super- $\delta$ -solvus domain. The forging domain is chosen with respect to the targeted final properties. In this study, the super- $\delta$ -solvus domain is only considered. During the hot forging, as soon as the  $\delta$  phase is dissolved, the microstructure is only composed by the austenitic matrix of nickel (FCC).

Through hot forging, dynamic recrystallization phenomena are overlapped by a classical hardening deformation process. For INCONEL 718, the dynamic recrystallization mechanism was characterized as a discontinuous process (see for instance, Wang et al. [2]). Some authors [3-4] report a necklace dynamic recrystallization process, depending on the deformation rate and the temperature compatible with a discontinuous behaviour of the dynamic recrystallization. Recrystallization is characterized by two processes: nucleation and growth. The nucleation process creates new grains with low dislocation densities. The grain growth process corresponds to grain boundaries motion, depending on the dislocation density and on misorientation

between adjacent grains. These phenomena act to minimize the total stored energy in the system.

Usually, an industrial hot forging is a multipass process. In this case, additional parameters must be taken into account: the number of passes, the interpass time and the temperature evolution during the deformation steps and the interpass time. The number of parameters is reduced when isothermal hot forging is performed. The literature gives many results for INCONEL 718 behaviour during a single pass hot deformation in the super- $\delta$ -solvus domain [1-7]. In the case of the super- $\delta$ -solvus domain, two papers only refer to multipass hot deformation [8-9]: the first study [8] was realized with an initial grain size of 250  $\mu\text{m}$  (1200°C / 7 hours) much larger than the present grain size. The second study [9] was performed in anisothermal conditions. For comparison, Ryan and McQueen [10] have studied an austenitic 316 stainless steel in multipass conditions.

The modelling proposed in this study takes into account the competition between hot hardening and dynamic recrystallization during both single pass and multipass processes. The evolution of the mechanical behaviour as well as the evolution of the microstructure of INCONEL 718, are computed. The numerical results are compared to the experimental observations. This study performed at the grain scale level, sequentially couples a deformation model (Cristal\_ECP) to a recrystallization model (CA\_ReX). The simulations are performed on a Representative Elementary Volume (3D aggregate) obtained by a superposition of EBSD mappings.

The deformation model, developed for large finite strains, is based on the continuous theory of dislocations and micro-plasticity mechanisms. It is implemented in the finite element ABAQUS code. This model estimates the amplitude and the distribution of local mechanical fields within the aggregate (see Hoc et al. [11] and Eriau et al. [12]).

The recrystallization model is a 3D cellular automaton code. The model predicts the grain nucleation and the migration of grain boundaries. It takes into account of the local variation of stored energy and of the topological effects. The approach was already used by Thébault et al. in 2008 and Solas et al. in 2009 for UDIMET 720 [13, 14].

### Experimental procedure

The laboratory samples were cut out from a 150 mm-diameter forged billet. Cylindrical specimens (12 mm in diameter and 18 mm long) were machined from the mid-radius of the billet.

Right before forging, the sample microstructure at high temperature (Figure 2(b)) was different from the as received microstructure (Figure 2(a)). To determine the former microstructure, different samples were submitted to the forging temperature during several dwell times, then helium quenched. According to literature, homogeneous temperature within the whole sample is predicted to be reached for a dwell time equal to one half hour by inch of diameter. For the laboratory sample geometry, the dwell time corresponded to fifteen minutes. The resulting microstructure, named initial microstructure, is shown in Figure 2(b). The grain size grew from 15  $\mu\text{m}$  (as received material) up to 95  $\mu\text{m}$  before forging.

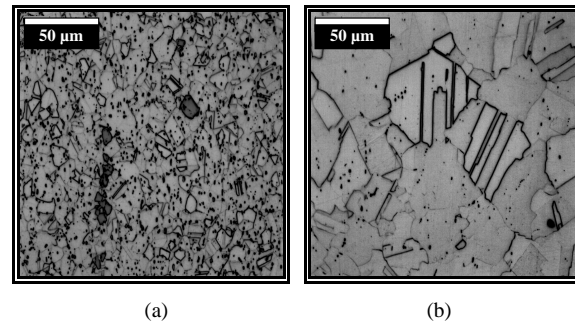


Figure 2: Optical micrographs of the microstructures (the compression axis is vertical), (a) as received material and (b) initial microstructure obtained after 15mn dwell time

Isothermal compression tests were performed on a hydraulic MTS press with a maximum loading of 50 T. This press was coupled to a lamp heating furnace allowing a maximum temperature of 1200°C. The temperature control was realized with a thermocouple welded on the sample surface.

Starting from the microstructure of the Figure 2(b), an isothermal compression was performed at a  $10^{-1} \text{ s}^{-1}$  constant deformation rate. Three different deformation paths were investigated: a single pass process (SP), a multipass process with an intermediate dwell time of ten seconds (MPD), and a multipass process containing an intermediate quench, a reheating and a fifteen minute holding period before the second compression (MPQ). These thermo-mechanical paths are sketched in Figure 3 at  $T > T_{\delta\text{solvus}}$ .

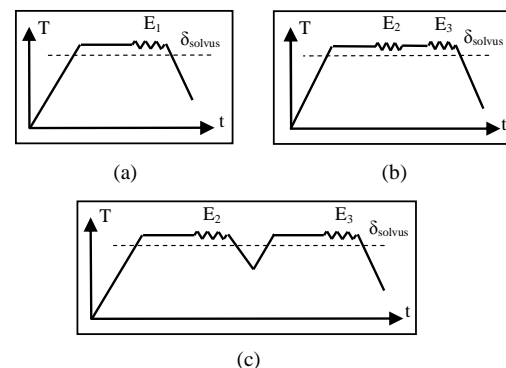


Figure 3: Thermo-mechanical cycles of the samples, (a) the SP process, (b) the MPD process and (c) the MPQ process

The thermo-mechanical paths had to comply with two main rules. Firstly, the sum of each macroscopic deformation step in the MPD and in the MPQ process ( $E_2 + E_3$ ) had to be equal to the total deformation in the SP process ( $E_1$ ). Secondly, for the MPD and MPQ processes, the strain value  $E_2$  had to be higher than the strain value  $E_3$  ( $E_2 > E_3$ ). For this study, the deformation rates were  $E_1 = 0.70$ ,  $E_2 = 0.40$  and  $E_3 = 0.30$  respectively.

For optical and Scanning Electron Microscopy (SEM) observations, each sample was then cut along their radius and mechanically polished. To reveal grain boundaries, a mechanical-

chemical polishing was performed on the samples with MASTERMET® (non-crystallized colloidal silica). The microstructures (mean grain size, twin fraction, sub-boundaries fraction...) were characterized at the end of each process, using an EBSD method coupled to a SEM FEG. A careful attention was paid to the location of the observed areas: all EBSD maps were performed on the sample core on a surface of  $1 \times 1 \text{ mm}^2$ , with an analysis step size of  $1 \mu\text{m}$ .

## Experimental results

### Mechanical behaviour

The mechanical behaviour during hot compression is plotted in Figure 4 for the three deformation paths.

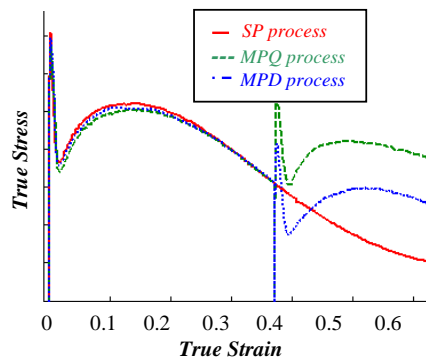


Figure 4: INCONEL 718, compression curve for a  $10^{-1} \text{ s}^{-1}$  strain rate

The compression curves (Figure 4) present an initial stress peak for the first pass (SP, MPQ and MPD) as well as for the second pass (MPQ and MPD). According to a previous study [5], these peak stresses result from the competition between the dislocation mobility and solute atoms. It should be noted that the three first pass curves are similar. For a strain value above 0.40, the SP, MPQ and MPD mechanical processes behave differently. Compared with the MPQ and MPD processes, the stress level corresponding to the SP process is smaller. Such SP curve corresponds to a maximal time of dynamic recrystallization and by extrapolation to a minimal dislocation density. To emphasize these behaviour differences, the hardening rate is plotted as a function of the true strain (Figure 5).

In the first pass, a transition between two linear ratings is observed. These ratings are represented by dashed lines in Figure 5. The first linear rating is identified as a work hardening and the second as a meta-stable equilibrium in the competition between the work hardening and the dynamic recrystallization. A previous analysis proved that this transition starts from  $E \approx 0.06$  for a lower deformation rate on the same material. It has been shown that this transition corresponds to the nucleation of recrystallized grains [15]. This result will be used in the numerical part of this study. The same transition is observed during the second pass on the MPQ sample. On the contrary, the MPD sample does not exhibit this transition. From these observations, it can be concluded that the microstructure is reinitiated during the interpass of the MPQ process. Its mechanical behaviour is controlled by the work

hardening, the nucleation of recrystallized grains and the grain growth. The lack of transition in the MPD sample can be explained as follows: this interpass of ten seconds is too short to fully recrystallize the microstructure and nuclei are still present at the beginning of the second pass. As a consequence, the MPQ stress level is almost the same in both passes.

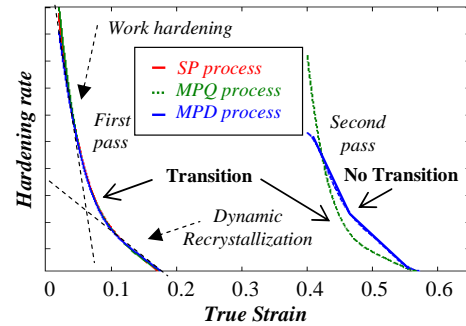


Figure 5: Evolution of hardening rate depending of the true strain in INCONEL 718 ( $10^{-1} \text{ s}^{-1}$ )

### Microstructural evolution

The EBSD method characterization was performed on four different quenched samples at different stage of each process (Figure 6).

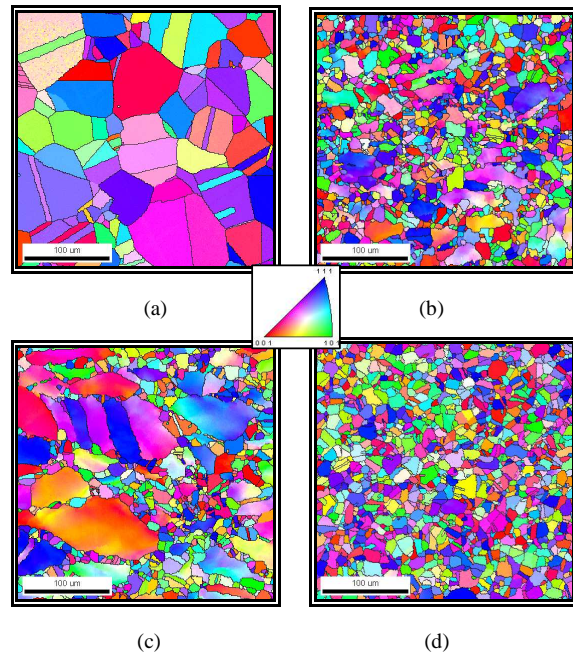


Figure 6: Material orientations maps from: (a) initial state, (b) SP process, (c) MPQ process and (d) MPD process

The first microstructure (Figure 6(a)) was obtained before forging and corresponded to the initial microstructure (Figure 2(b)). The

other three microstructures (Figures 6(b), 6(c), 6(d)) corresponded to the end of each process, i.e, at a total  $E = 0.70$ . The different microstructure features are given in Table 1.

Table 1: Quantitative results obtained from EBSD data

	Grain Size ( $\mu\text{m}$ )	Sub-boundary ratio (%)	Twin ratio (%)
As received	15	25	30
Initial (Dwell)	95	5	55
SP process	25	25	15
MPQ process	55	35	15
MPD process	20	10	25

EBSD data corresponding to the grain size, the sub-boundary ratio and the twin ratio of the different quenched microstructures are given in Table 1. Quenching froze the microstructure and stopped grain boundary migration. It should be noted that the grain size of the as received state was 5 times lower than the dwell microstructure grain size. Moreover, the sub-boundary ratio was divided by a factor five, whereas the twin ratio was multiplied by a factor two. These analyses pointed out a growth phenomenon related to static recrystallization during the fifteen minutes dwell time before the first pass.

After a 0.70 total deformation, the final grain size and twin ratio decreased, compared to the initial microstructure. The twin ratio evolution means that twins cannot grow during dynamic recrystallization. This assumption agrees with the literature results. According to Gleiter's atomistic model [16], the formation of annealing twins can be explained by a nucleation process on the  $\{111\}$  planes on the growing grains. Nucleation twin process induces new crystallographic orientations within the microstructure. Two grains separated by a twin underwent different plastic and lattice rotations with increasing applied strain and the twin misorientation conditions progressively disappeared above a 0.70 strain. Such phenomenon explains the decrease of the twin ratio after the different processes. Moreover, observations showed that the final sub-boundary ratio was always higher after deformation.

Mechanical behaviour of the final specimens being strongly dependent on the microstructure, a model is now proposed to understand the origin of these microstructures.

### Numerical models

Two models are coupled and successively used: first, the polycrystalline model, implemented in a Finite Element code, computes the lattice rotation field, the local strain and stress fields and the dislocation density at each Gauss point of the grain meshing, for a fixed time increment. The new crystallographic orientation and dislocations densities within the grains are implemented within the cells (sites) of a 3D cellular automation. Next, the recrystallization model computes the probability for a site to be recrystallized (nucleation and growth) and determines the new crystallographic orientation and the new dislocation densities for recrystallized sites. These new data are implemented in the polycrystalline model for a new cycle. A step N is defined by a calculation with the polycrystalline modelling followed by a calculation with the recrystallization model.

### Crystalline plasticity model: Cristal ECP

The polycrystalline model rests on the continuous theory of dislocations and on the framework of the finite transformations. The model is implemented in the Finite Element codes ABAQUS® and CAST3M®. Each grain of the polycrystal is meshed and each point of the meshing follows the hereafter crystalline plasticity laws.

Each grain of the polycrystal is considered as a single crystal. At any Gauss point of a given grain, the local plastic behaviour is described in terms of dislocation densities on the slip systems. For the chosen forging temperature, INCONEL 718 is a single phase material. The austenitic nickel matrix has a FCC structure and twelve conventional slip systems  $\{111\}\langle 110 \rangle$ . The Schmid's criterion which rules the activation of the different slip systems  $s$  is given by:

$$|\tau^s| \geq \tau_c^s \quad (1)$$

where  $\tau^s$  is the resolved stress on the slip system  $s$  and  $\tau_c^s$  the critical shear stress on the same slip system.

The constitutive visco-plastic law is given by:

$$\frac{\dot{\gamma}^s}{\dot{\gamma}_0} = \left| \frac{\tau^s}{\tau_c^s} \right|^m \quad (2)$$

where  $\dot{\gamma}^s$  is the slip rate on the slip system  $s$ ,  $m$  is the strain rate parameter.

The critical resolved shear stress  $\tau_c^s$  on the system  $s$  is given by:

$$\tau_c^s = \tau_0 + \mu b \sqrt{\sum_t a^{st} \rho^t} \quad (3)$$

where  $\tau_0$  depends on the lattice friction and on interactions with solute atoms,  $\sum_t \rho^t$  is the total dislocation density on the twelve slip systems,  $\mu$ ,  $b$  are respectively the shear modulus, the Burgers vector magnitude and  $a^{st}$  is a component of the interaction matrix between the slip systems  $s$  and  $t$ .

The dislocation density evolution corresponds to the Kocks and Mecking hardening law. It is composed of two terms: a production term based on Orowan's relationship (i.e. proportional to the mean free path of mobile dislocations  $L^s$ ) and an annihilation term  $g_c \cdot \rho$  which takes into account the dynamic recovery during deformation.

$$\dot{\rho}^s = \frac{|\dot{\gamma}^s|}{b} \left( \frac{1}{L^s} - g_c \rho^s \right) \text{ with } \frac{1}{L^s} = \frac{1}{D} + \sqrt{\frac{\sum_{t \neq s} \rho^t}{K}} \quad (4)$$

Only self hardening  $a^{ss}$  and latent hardening  $a^{st}$  are considered here. The physical meaning of all the parameters set is detailed in [17].  $D$  is the initial grain size assuming that a twin boundary is a classical boundary and  $L^s$  is the mean free path and  $K$  is a material parameter.

At the forging temperature, material parameters  $b$  and  $a^{st}$  were determined from the literature data for UDIMET 720 (Thébault et al. [13]). Parameters  $m$  and  $D$  were determined by inverse method from experimental tests. The  $\tau_0$ ,  $g_c$ ,  $\rho_0$ ,  $K$  and  $\dot{\gamma}_0$  parameters were identified by the Gauss-Newton algorithm [18]. The material parameters used in this study are given by Table 2.

At each Gauss point of the meshing, for a given applied strain, the polycrystalline model gives the local stress, strain, lattice rotation fields and the dislocation density. The misorientation between two points of a same grain corresponds to deformation sub-grain boundaries.

#### Recrystallization model: CA ReX

The above FE polycrystalline model does not contain any recrystallization phenomenon. To describe nucleation and grain growth, a second model is implemented in a 3D cellular automaton code and coupled to the deformation model. The recrystallization model uses the dislocation density computed by the deformation model. After each step of deformation, the FE polycrystalline model produces local gradient of dislocation density and intragranular crystallographic reorientations. It gives at each point of the FE meshing the total local dislocation density  $\rho$ . These data are implemented at each site of the cellular automaton.

Nucleation occurs at high stored energy sites. The density of stored energy is given by:

$$E_{stored} = \frac{1}{2} \mu b^2 \sum_t \rho^t \quad (5)$$

For dynamic recrystallization, the classical criterion, based on stored energy, gives a too large number of nuclei. In this paper a new criterion resting on nucleation probability  $P_n$  is proposed:

$$P_n = 1 - \exp\left(-\frac{\sum_t \rho^t}{\rho_n}\right)^n > P \quad (6)$$

where  $\rho_n$  is a dislocation density parameter determined from the deformation model and  $n$  is a material parameter.  $\rho_n$  and  $n$  are identified (see Table 2). As soon as the criterion given in equation (6) is achieved, i.e the nucleation probability  $P_n$  is higher than a random number  $P$ , the site (or element) will obtain a minimal dislocation density  $\rho_0 = 1.2 \cdot 10^4 \text{ mm}^{-2}$  and the site will keep its orientation. To grow, a nucleus or an already recrystallized site must be present. This condition is satisfied when the dislocation density is lower than a threshold value  $\rho_g$  (its identified value is given in Table 2). This value is larger than  $\rho_0$ : a site which was

recrystallized at N-1 cycle and submitted to low deformation at cycle N, can grow during the recrystallization at cycle N.

The velocity of the grain boundary between  $s$  and  $s'$  sites depends on the mobility  $M^{ss'}$  of the interface. The growth rate is given by:

$$V = -M^{ss'} \Delta E \quad (7)$$

The boundary mobility between the site  $s$  and its neighbour  $s'$  is determined by:

$$M^{ss'} = M_m \left[ 1 - \exp\left(-\left(\frac{\theta^{ss'}}{10}\right)^3\right) \right] \quad (8)$$

The driving force  $\Delta E$  corresponds to the variation in the system energy, between the initial and final configuration. The driving force consists of two terms:

$$\Delta E = \Delta E_{gb} + \Delta E_{stored} \quad (9)$$

$\Delta E_{stored}$  is the variation in stored energy obtained from the density dislocations.

$\Delta E_{gb}$  is the variation in boundary energy associated with the change of orientation associated to the migration of the grain boundaries:

$$E_{gb} = \sum d^{ss'} \gamma^{ss'} \quad (10)$$

where  $d^{ss'}$  is the distance between a site and its neighbors and  $\gamma^{ss'}$  is obtained from Read and Shockley equation:

$$\gamma^{ss'} = \begin{cases} \gamma_m \frac{\theta^{ss'}}{\theta^*} \left[ 1 - \ln\left(\frac{\theta^{ss'}}{\theta^*}\right) \right] & \text{when } \theta^{ss'} \leq \theta^* \\ \gamma_m & \text{when } \theta^{ss'} > \theta^* \end{cases} \quad (11)$$

When the driving force is positive, the site retains its initial configuration (orientation and stored energy). When the driving force is negative, the probability of reorientation can be computed. This probability is the distance  $d$  traveled by the grain boundary within a cell  $d_0$  over an increment of time  $t_{inc}$ :

$$P^{ss'} = \frac{d}{d_0} = \frac{-V t_{inc}}{d_0} = \frac{-M^{ss'} \Delta E t_{inc}}{d_0} > P \quad (12)$$

For each site, this probability is calculated with the six possible reorientations. The reorientation with the highest probability is chosen. The microstructure is updated once all probabilities have been calculated, and only those sites with probabilities over a random number are effectively reoriented. The Equation 12 parameters are determined by two methods which correspond to the deformation model results ( $\rho_n$  and  $\rho_g$ ), and to the literature ( $M_m$  and  $\gamma_m$ ) [13], as shown in Table 2.

Table 2: Material parameters identified in this study taken from Cristal\_ECP and CA\_ReX

	b (nm)	a <sup>st</sup>	v	E (GPa)	m	D (μm)	τ <sub>0</sub> (MPa)	g <sub>c</sub> (nm)	ρ <sub>0</sub> (mm <sup>-2</sup> )	K	$\dot{\gamma}$ (s <sup>-1</sup> )	M <sub>m</sub> (m <sup>4</sup> J <sup>-1</sup> .s <sup>-1</sup> )	γ <sub>m</sub> (J.m <sup>-2</sup> )	ρ <sub>g</sub> (mm <sup>-2</sup> )	ρ <sub>n</sub> (mm <sup>-2</sup> )	n
γ <sub>matrix</sub>	0.26	8e <sup>-3</sup>	0.3	105	0.23	44	5	28	1.0e <sup>7</sup>	21	1.3e <sup>-4</sup>	2e <sup>-10</sup>	0.05	1.3e <sup>8</sup>	2.5e <sup>8</sup>	7.5

#### Aggregate construction and boundary conditions

Two three-dimensional aggregate types are used in this study. The first one is a cubic aggregate with random orientations (Euler's angles) determined from the equation (13):

$$\begin{aligned}\varphi_1 &= \text{random}[0, 2\pi[ \\ \phi &= a \cos(\text{random}[-1, 1]) \\ \varphi_2 &= \text{random}[0, 2\pi[ \end{aligned} \quad (13)$$

This aggregate is composed of 64,000 elements and 1,000 grains. It gives the best trade off between the computation time and the computing storage. A simulated compression test up to  $E \approx 0.70$  can be performed in less than ten hours with a parallelization on eight processors. This aggregate is used in parameter identification. The second 3D aggregate is a Representative Elementary Volume (REV) of the material microstructure. It was obtained using the Rey et al. procedure [19]. The microstructure was obtained from EBSD mapping. Figure 7 shows a screenshot of these aggregates taken from the FE code CAST3M®.

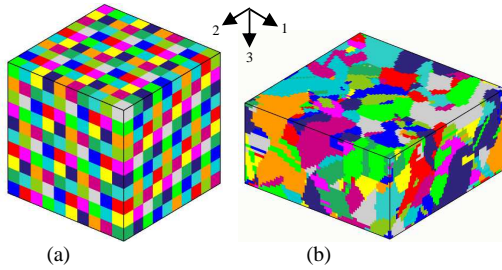


Figure 7: Microstructures of the aggregates, (a) the random aggregate and (b) the actual aggregate

The objective of these aggregates is to construct a model of the forging process. It is possible to consider the forging as a simple compression test. A previous study led by Schwartz et al. [20] allows determining the best boundary conditions to apply in order to realize compression test (Figure 8).

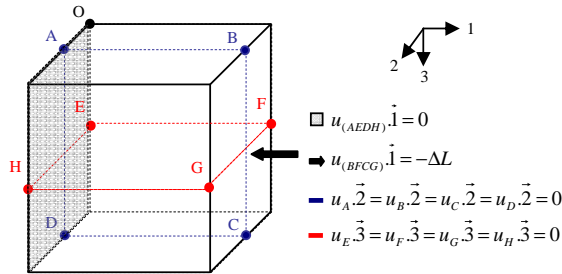


Figure 8: Boundary conditions of the aggregates

The REV is composed of thirty layers of grains, with a 10 μm step between two layers. The total dimensions of this aggregate are 600x600x300 μm<sup>3</sup> divided into 75x75x30 elements with a total of 168,750 elements. The aggregate used contains 3,189 grains.

#### Modelling results

This coupled approach corresponds to a macroscopic dynamic recrystallization where deformation portion is ensured by the polycrystalline model and the recrystallization portion by the recrystallization model described above. For such a coupling, a coherent determination of a characteristic time for both models is required. In the present case, for each simulated cycle, the deformation and recrystallization times ( $t_{inc}$ ) are similar.

The simulation results highlight three features: the comparison between experimental and numerical mechanical behaviour for SP process, the analysis of the dislocation density evolution during the modelling of SP process and the application for the multipass processes considering interpass effects. Only results obtained from the actual aggregate are presented, either on mechanical behaviour or on dislocation density evolutions.

#### Mechanical behaviour

Seventeen deformation-recrystallization cycles are performed up to a 0.70 final deformation; the first step corresponds to a 0.075 deformation increment, the others are similar with a 0.025 increment. It should be noted that the identification of the material parameters of the polycrystalline model were determined during the first deformation step, since it was previously proved that no dynamic recrystallization occurred for a deformation less than 0.06 [15]. Experimental and numerical stress-strain curves are given in Figure 9.

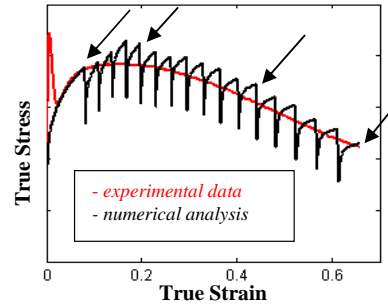


Figure 9: Comparison between experimental and numerical mechanical behaviour obtained from the actual aggregate modelling the SP process

Ignoring the initial peak stress, the estimated stress is in good agreement with experimental results. The stress level, obtained



during the seventeen numerical steps, oscillates around the experimental stress curve up to a 0.70 deformation.

#### Dislocation density evolution in the SP process

The distribution of the dislocation densities in the actual aggregate meshing is given in Figure 10. The four analysed steps correspond to the end of the first deformation step ( $\varepsilon_1 \approx 0.075$ ), to the ends of the fifth step ( $\varepsilon_5 \approx 0.19$ ), of the twelfth step ( $\varepsilon_{12} \approx 0.43$ ) and of the seventeenth step ( $\varepsilon_{17} \approx 0.70$ ).

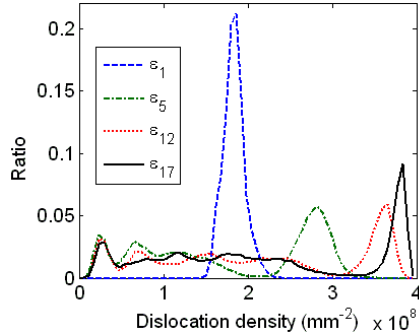


Figure 10: Dislocation density distribution evolution obtained from the actual aggregate modelling the SP process

The probability curves show a wavy background and some major peaks located at the end of each step corresponding to a large amount of sites presenting large dislocation densities. The criterion used for recrystallization initiation rests on a critical dislocation density  $\rho_n = 2.5 \cdot 10^8 \text{ mm}^{-2}$ . For  $\varepsilon_1$ , the major peak corresponds to a  $2 \cdot 10^8 \text{ mm}^{-2}$  dislocation density and according to only equation (6), 100% of sites are potential nuclei.

For  $\varepsilon_5 \approx 0.19$ , the highest peak corresponds to the maximum stress of the stress-strain curve. This peak means that 30-40% of the sites present an average density dislocation  $\rho_5 \sim 3 \cdot 10^8 \text{ mm}^{-2}$  with a start of recrystallization on some sites. Each small peak corresponds to sites having experienced a former recrystallization during the steps 1 to 4.

The step  $\varepsilon_{12} \approx 0.40$  corresponds to the end of the MPD and MPQ first pass (see Figure 4). The curve  $\varepsilon_{12}$  presents a constant background ending by one peak corresponding to a large amount of sites (30%) with an average value  $\rho_{12} \sim 3.5 \cdot 10^8 \text{ mm}^{-2}$ . It should be noted that  $\rho_{12} > \rho_5$ . For SP process, the step  $\varepsilon_{17}$  is similar to the distribution curve  $\varepsilon_{12}$ . After recrystallization, the local strain of the sites presenting large  $\rho$  values decreased. These results confirm the tendency for deformed sites to disappear in favour of recrystallized sites.

#### Multipass process

For the three processes, simulations of the evolution of the microstructures (Figure 11) and dislocation density distributions (Figure 12) are given for 5 steps:  $\varepsilon_1 = 0.075$ ,  $\varepsilon_5 = 0.19$ ,  $\varepsilon_{11} = 0.40$ ,  $\varepsilon_{12} = 0.43$  and  $\varepsilon_{17} = 0.70$ . Each step corresponds to one deformation followed by one recrystallization and is depending on results obtained from the former steps. The orientation maps are represented by a simplified microstructure within the initial

configuration. In such a representation, a grain is sketched by a cube (or for 2D maps, represented by a square). Each cube contains 64 sites whereas each square contains 16 computation sites (or Gauss points). A nucleus is represented by a small square with similar or different crystallographic orientation according to the nucleation criterion. All maps correspond to the central layers of the aggregate.

These figures highlight the differences between the microstructures as well as the differences between the dislocation densities obtained after the SP, MPQ and MPD processes. As the nuclei orientation has been assumed to be the same as the parent grain, no distinct nucleus can be seen on the orientation maps.

The three processes having a common deformation path up to  $\varepsilon_{11} = 0.40$ , the microstructure evolutions are similar for  $\varepsilon_1$  to  $\varepsilon_{11}$  (Figure 11(a) to Figure 11(c)). For  $\varepsilon_{12}$  to  $\varepsilon_{17}$ , large differences are obtained between SP process (0.25s interpass time), MPD process (10s interpass time) and MPQ process (15mn interpass time), as it can be seen in Figure 11(d), to Figure 11(i).

For the first deformation step  $\varepsilon_1$ , a gradient of orientation (represented by a gradient of colour) appears in some grains. See, for example, the grain at the bottom of Figure 11(a) (indicated by the black arrow).

For the 5<sup>th</sup> deformation step ( $\varepsilon_5$ ) corresponding to Figure 11(b), growth of few grains are observed for the first time. Moreover, the gradient of orientation increases with applied deformation in most of the grains. New orientation of the nuclei (small squares within the grains) can be observed.

For the 11<sup>th</sup> deformation step ( $\varepsilon_{11}$ ), the gradient of orientations inside grains are higher than previously (Figure 11(c)). A site with a new orientation can be seen at the bottom of the figure (pointed by black arrow); no nucleus being visible, the new site orientation results of the growth of a grain lying in the upper or lower layer. This result emphasises the 3D interactions between the grains of the aggregate.

The deformed grains develop a  $\langle 110 \rangle$  fiber texture parallel to the compression axis. Nevertheless, as nucleation of annealing twins is not yet introduced in the model, the randomization of grain orientation associated to the evolution of recrystallized grains is not observed [22].

Let us come back to the SP process. Figures 11(c), 11(d) corresponding to  $\varepsilon_{11}$  and  $\varepsilon_{12}$  respectively show little evolution of the orientation maps. At the 17<sup>th</sup> step ( $\varepsilon_{17}$ ) a duplex microstructure is pointed out. This microstructure is composed of grains with a large gradient of orientation (deformed grains) and grains without gradient (recrystallized grains). This result agrees with the experimental microstructure observed in Figure 6(b).

Figures 11(e) and 11(h) reveal the evolution of the microstructure due to the MPQ process for  $\varepsilon_{12}$  and  $\varepsilon_{17}$ . Compared to Figure 11(c), a dwell time of fifteen minutes induces post-dynamic recrystallization and grain growth. Small differences are observed between  $\varepsilon_{12}$  and  $\varepsilon_{17}$ . These numerical results point out that this MPQ process lead to a re-initialization of the microstructure before the second pass. For  $\varepsilon_{12}$  and  $\varepsilon_{17}$ , the computed microstructures being close.

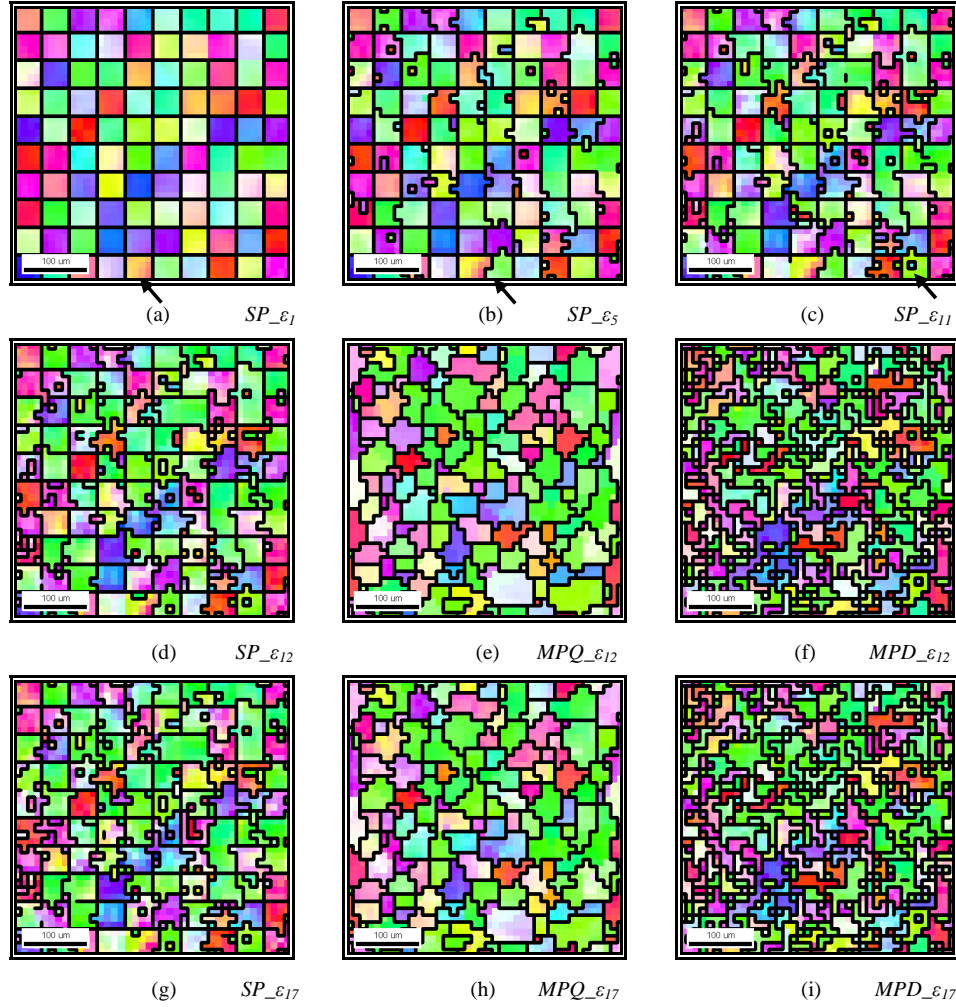


Figure 11: Orientation maps from the modelling, (a) after the first deformation, (b) after the fifth deformation, (c) after the eleventh deformation, (d) after the twelfth deformation with the SP process, (e) after the twelfth deformation with the MPQ process, (f) after the twelfth deformation with the MPD process, (g) after the seventeenth deformation with the SP process, (h) after the seventeenth

These numerical results point out that this MPQ process led to a re-initialization of the microstructure before the second pass. For  $\epsilon_{12}$  and  $\epsilon_{17}$ , the computed microstructures being close. The dwell period has a significant effect on the distribution of dislocation densities of MPD and MPQ processes (Figure 12).

For MPQ process, simulations reveal a large decrease of dislocation density, when compared to SP process. At  $\epsilon_{12}$  step, the sites corresponding the background can grow as soon as the growth criteria  $\rho_g = 1.3 \cdot 10^8 \text{ mm}^{-2}$  is achieved. For  $\epsilon_{17}$ , most of the sites can grow. For the MPQ process at  $\epsilon_{12}$ , the dislocation density distribution is similar to the one obtained after the  $\epsilon_5$  step with the SP process. This confirms that the deformation level is low during the second pass of the MPQ process and the sample is partly recrystallized. As a conclusion, the simulation of the MPQ process agrees with experimental observations.

For the MPD process, the evolution of the crystallographic orientation is given in Figure 11(f) and in Figure 11(i). The microstructure obtained for  $\epsilon_{12}$  step, is intermediate between the SP and MPQ microstructures. During the 10s interpass time, an important boundary migration occurs due to the meta-dynamic recrystallization phenomenon. According to Figure 12, almost 20% of the sites have a dislocation density above the growth criteria  $\rho_g$ : the structure is not fully recrystallized.

As a consequence, after the twelfth deformation, the dislocation density distribution with the MPD process is intermediate between the SP and the MPQ processed. During the short interpass time, the recrystallized sites can grow, but some deformed areas remain in the microstructure. These features explain the different work hardening rates observed with the three thermo-mechanical cycles.



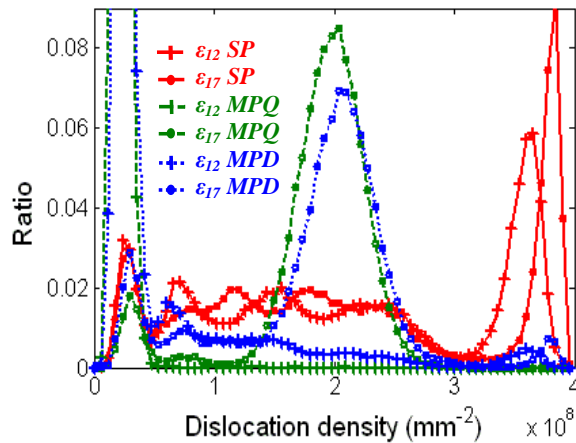


Figure 12: Comparison of the evolution of the dislocation density distribution at different stages of the SP, MPQ and MPD processes. Simulations are performed via the actual aggregate

### Conclusions

An experimental study on INCONEL 718 allows stress-strain curves to be determined during three different hot forging processes. The microstructure evolution has been studied during these processes and linked with mechanical behaviour up to a 0.70 deformation:

- 1/ The single pass process exhibits the lowest final stress level and an heterogeneous grain size distribution.
- 2/ The multi-pass quench process shows the highest final stress level and an heterogeneous grain size distribution owing to the microstructure re-initialization during the interpass.
- 3/ The multi-pass dwell process leads to an intermediate final stress level and an homogeneous grain size distribution due to short interpass time keeping nuclei from the first pass.

A new numerical simulation, compared with experimental results, is used to predict the mechanical behaviour and microstructure evolution of INCONEL 718 during multi-pass hot forging. This modelling is achieved by a coupling between a crystalline plasticity model and a recrystallization model. The numerical coupling enables the linking of the 3D interactions between grains of the aggregate. The numerical results are in good agreement with the experience. The approach enables to determining of the part of the different mechanisms (plasticity and recrystallization) at the origin of the different microstructure evolutions as well as the mechanical behaviour during complex multipass processes.

### Acknowledgments

This work was supported by Forges de Bologne which has provided the material. The authors thank Nicolas Roubier from MSSMat/ECP for his many contributions during this effort.

### References

[1] M.S Lewandowski and R.A Overfelt, "High temperature deformation behaviour of solid and semi-solid alloy 718", *Acta mat.*, 47 (1999) 4695-4710.

[2] Y. Wang, et al., "Microstructure evolution during dynamic recrystallization of hot deformed superalloy 718", *Mat. Sc. And Eng.*, 486 (2008) 321-332.

[3] J.M Zhang et al., "Mathematical modeling of the hot deformation behavior of superalloy IN718", *Met. and Mat. Trans.*, 30A (1999) 2701-2712.

[4] H. Yuan and W.C Liu, "Effect of the  $\delta$  phase on the hot deformation behaviour of Inconel 718", *Mat. Sc. And Eng.*, 408 (2005) 281-289.

[5] A.A Guimaraes and J.J Jonas, "Recrystallization and aging effects associated with the high temperature deformation of Waspaloy and Inconel 718", *Met. Trans.*, 12A (1981) 1655-1666.

[6] S.C Medeiros et al., "Microstructural modeling of metadynamic recrystallization in hot working of IN 718 superalloy", *Mat. Sc and Eng.*, 293 (2000) 198-207.

[7] A. Thomas et al., "High temperature deformation of INCONEL 718", *J. Mat.Proc. Tec.*, 177 (2006) 469-472.

[8] M.C Mataya, "Simulating microstructural evolution during the hot working of alloy 718", *JOM*, (1999) 18-26.

[9] N.K Park et al., "Hot forging of a nickel-base superalloy", *J. of Mat. Proc. Tec.*, 111 (2001) 98-102.

[10] N.D Ryan, H.J McQueen, "Hot strength and microstructural evolution of 316 stainless steel during simulated multistage deformation by torsion", *J. Mater. Proc. Tech.*, 36 (1993) 103-123.

[11] T. Hoc, C. Rey and J. Raphanel, "Experimental and numerical analysis of localization during sequential tests for IF-Ti steel", *Acta metall materialia*, 49 (2001), 1835-1846.

[12] P. Eriau and C. Rey, "Modelling of deformation and rotation bands and of deformation induced grain boundaries in IF steel aggregate during large plane strain compression", *Inter.J. Plast.*, 20 (2004), 1763-1788.

[13] J. Thébault et al., "Polycrystalline modelling of Udimet 720 forging", *Superalloys*, 11 (2008) 985-992.

[14] D. Solas et al., "Dynamic recrystallization modeling during hot forging of a nickel based superalloy", *Materials Science Forum*, 638-42 (2010) 2321-2326.

[15] J. de Jaeger et al., "INCONEL 718 recrystallization in the delta supersolvus domain", *Advanced Materials Research*, 409 (2011) 751-756.

[16] H. Gleiter, "The formation of annealing twins", *Acta Met.*, 17 (1969) 1421-1428.

[17] J. Thébault, "Etudes expérimentale et numérique des mécanismes de déformation et de recristallisation de l'UDIMET 720 lors du forgeage. Relations entre la microstructure et la

perméabilité aux ultrasons" (Ph.D. thesis, Ecole Centrale Paris, 2009), 105-162. (<http://hal.archives-ouvertes.fr>)

[18] J. Nocedal and S. J. Wright, "*Numerical Optimization*", (Springer series in operations research, 2006), 227-253.

[19] C. Rey, D. Solas and O. Fandeur, "*Grain boundaries and crystalline plasticity*", (Ed. L. Priester, ISTE, WILEY, 2011), 109-163.

[20] J. Schwartz, "Approche non locale en plasticité cristalline : application à l'étude du comportement mécanique de l'acier AISI 316LN en fatigue oligocyclique" (Ph.D. thesis, Ecole Centrale Paris, 2011), 125-159. (<http://hal.archives-ouvertes.fr>)

[21] P. Peczak and M.J. Luton, "The effect of nucleation on dynamic recrystallization I. Homogeneous stored energy distribution", *Philosophical Magazine*, 68 (1993) 115-144.

[22] F.J. Humphreys and M. Hatherly, "*Recrystallization and related annealing phenomena*", (Elsevier Ltd Second Edition 2004), 393-403.